emerald PUBLISHING

International Journal of Numerical Methods for He
Flui

Topology optimisation of transient turbulent compressible flow

Journal:	*International Journal of Numerical Methods for Heat and Fluid Flow*
Manuscript ID	HFF-04-2026-0598
Manuscript Type:	Research Article
Keywords:	Fluid topology optimisation, Discontinuous Galerkin, Transient flow, Turbulent flow, Compressible flow

Topology optimisation of transient turbulent compressible flow

April 30, 2026

Abstract

Purpose - We present the first topology optimisation formulation for transient turbulent compressible flow modelled with the unsteady Favre-averaged Navier–Stokes equations.

Design/Methodology/Approach - The topology to be designed is incorporated in each of the momentum balance, the energy balance, and the turbulence closure. The forward and adjoint equations are implemented with different discretisations: the forward model with a finite volume method, and the adjoint model with a discontinuous Galerkin finite element scheme, since the former is very robust and the latter can be adjoined automatically. Once discretised, the topology optimisation problem is solved with an integer linear programming algorithm. We demonstrate the capability of our approach in the design of a U-bend, a pipe joint, and a double pipe joint.

Findings - The formulation is developed and demonstrated through numerical examples, showcasing the developed approach.

Originality/Value - No previous topology optimisation formulation was available for transient turbulent compressible flow modelled with the unsteady Favre-averaged Navier–Stokes equations.

Keywords: Fluid topology optimisation; discontinuous Galerkin; transient flow; turbulent flow; compressible flow

1 Introduction

Topology optimisation of fluid flow devices was pioneered by Borrvall and Petersson (2003), in the context of stationary incompressible Stokes flows. Over the years the community has progressively extended this approach to more complex situations, including incompressible Navier–Stokes flows (Gersborg-Hansen *et al.*, 2005), non-Newtonian fluids (Pingen and Maute, 2010), thermal-fluid interactions (Yaji *et al.*, 2016), and incompressible turbulent flows (Papoutsis-Kiachagias *et al.*, 2011). These methods have been applied to many important engineering design problems, including for example, mixers (Andreasen *et al.*, 2009), arterial by-pass grafts (Zhang and Liu, 2015), bladed rotors (Romero and Silva, 2014), fluid diodes (Lin *et al.*, 2015), and rectifiers (Jensen *et al.*, 2012). Fluid compressibility, which is crucial to consider when changes in density cannot be neglected, makes the system of partial differential equations (PDEs) much more complicated to solve, as mechanical and thermodynamic effects are tightly coupled (Sá *et al.*, 2021). In particular, a dependence on the density arises in all balance equations, which depends on the thermodynamic state of the fluid. The first work considering compressible flow was for laminar subsonic conditions (Sá *et al.*, 2021), and was further explored by Okubo *et al.*, (2022), with a different approach for the adjoint model, and by Maffei *et al.*, (2023), with an integer programming approach. Each of these works on compressible equations considered the stationary case.

For some design problems this stationarity assumption is acceptable. However, for other problems, transient effects are crucial. A clear example is where the boundary conditions (such as the inlet flow rate) or domain boundaries are time-dependent. Topology optimisation for transient problems has been confined to laminar incompressible flows (Kreissl *et al.*, 2011; Deng *et al.*, 2011) with body forces (Deng *et al.*, 2013) and heat transfer (Makhija and Beran, 2019), and to laminar compressible flows (Alonso *et al.*, 2025).

Many design problems involve turbulence. In this work we employ the UFANS (Unsteady Favre-averaged Navier–Stokes) equations, which are the compressible flow version of the URANS (Unsteady Reynolds-averaged Navier–Stokes) equations (Pope, 2000; Wilcox, 2006). This framework solves time-dependent equations for the mean fields of all prognostic variables. These equations are not closed, because the mean-field equations incorporate terms describing the influence

of the unknown turbulent fluctations. These unknown Reynolds stresses/turbulent heat flux terms are modelled with different turbulence closure models. In topology optimisation, several turbulence models have already been considered for incompressible flow, including the Spalart–Allmaras model (Yoon, 2016), the k-ω model (Dilgen *et al.*, 2018), the k-ϵ model (Yoon, 2020) and the Wray–Agarwal model (Alonso *et al.*, 2022). For compressible fluids, the statistical averaging involves the density, which gives rise to the FANS (Favre-averaged Navier–Stokes) equations (Wilcox, 2006). In topology optimisation, this has been considered by Garcia Rodriguez *et al.*, (2025), formulating it for the compressible version of the Spalart–Allmaras turbulence model. In this work we employ the Wray–Agarwal model, which has some advantages from the point of view of topology optimisation.

We approximate the forward and adjoint equations with two different discretisations: a standard finite volume scheme implemented in OpenFOAM® (Weller *et al.*, 1998), and a discontinuous Galerkin (DG) method (Hartmann, 2006) implemented in FEniCS (Logg *et al.*, 2012) using `dolfin_dg` (Houston and Sime, 2018). This is essentially for software engineering reasons: the forward model of OpenFOAM® is extremely robust and has sophisticated devices to achieve convergence, but there is no adjoint model available; the DG discretisation in FEniCS offers an automatically-derived adjoint using the `dolfin-adjoint` library (Farrell *et al.*, 2013; Mitusch *et al.*, 2019), but lacks the subtle adjustments needed for robust convergence of the forward model. This approach combines the strengths of both codes (Alonso *et al.*, 2021). This choice means that the adjoint is not discretely consistent; nevertheless, the gradients obtained provide descent directions for the topology optimisation problem, and allow for its successful solution.

We formulate the forward model for an ideal gas. The formulation of the topology optimisation problem considers a continuous design variable and uses the classic Borrvall–Petersson material model for the inverse permeability (Borrvall and Petersson, 2003). The linear systems arising in the adjoint model are solved with UMFPACK (Davis, 2004). The optimisation problem is solved with a sequential integer linear optimisation algorithm (Souza *et al.*, 2021; Sivapuram and Picelli, 2018).

This paper is organised as follows: in Section 2, the formulation and DG discretisation used for the forward model are presented; in Section 3, the topology optimisation formulation is presented; in Section 4, the numerical implementation is described; in Section 5, some numerical results are shown; and in Section 6, some conclusions are drawn.

2 Formulation and DG discretisation of the forward model

There are essentially four equations that need to be considered: the continuity, momentum, energy and turbulence equations. The Wray–Agarwal turbulence model employed is a single-equation turbulence model that combines the advantages of the near-wall modelling from the k-ω model with the freestream modelling from the k-ε model (Wray and Agarwal, 2015), being also partly based on the SST k-ω model (Wray and Agarwal, 2015). Wray and Agarwal (2015) show that the Wray–Agarwal turbulence model leads to more accurate boundary layer separation predictions than the Spalart–Allmaras model, and that it is also competitive with the SST k-ω model for wall-bounded flows. Throughout the years, several evaluations, improvements and variations have been developed (Wray and Agarwal, 2016; Han *et al.*, 2017). Particularly, the 2018 version (referred in Han *et al.*, (2018) as WA2018) is considered. The main advantage of the 2018 version is that it does not rely on the computation of the wall distance. Not needing to compute the wall distance is advantageous from a topology optimisation point of view, because the wall distance computation requires an additional penalisation term (Yoon, 2016) in order to account for the modelled solid material, which must be calibrated (i.e., adequately chosen) for obtaining the optimised topology. An additional term to account for the attenuation of turbulence in the porous medium is included, as presented in Alonso *et al.*, (2022). Neglecting external body forces, the set of equations in conservative form is:

$$\frac{\partial \rho}{\partial t} + \nabla\cdot(\rho \boldsymbol{v}) = 0, \tag{1}$$

$$\frac{\partial (\rho \boldsymbol{v})}{\partial t} + \nabla\cdot[(\rho \boldsymbol{v}) \otimes \boldsymbol{v}] = \nabla\cdot(\boldsymbol{T} + \boldsymbol{T}_R) + \boldsymbol{f}_r(\alpha), \tag{2}$$

$$\frac{\partial (\rho e_{\text{total}})}{\partial t} + \nabla\cdot(\rho e_{\text{total}} \boldsymbol{v}) = \nabla\cdot[(k_{th} + k_{th,\text{T}})\nabla T_{\text{K}}] + \nabla\cdot[(\boldsymbol{T} + \boldsymbol{T}_R)\boldsymbol{v}], \tag{3}$$

$$\frac{\partial(\rho R_{\mathrm{T}})}{\partial t} + \nabla\cdot(\rho \boldsymbol{v} R_{\mathrm{T}}) = \nabla\cdot\left[(\sigma_R \rho R_{\mathrm{T}} + \mu)\nabla R_{\mathrm{T}}\right] + \rho C_1 R_{\mathrm{T}} S + f_1 C_{1,k\text{-}\omega}\rho\frac{R_{\mathrm{T}}}{S}\nabla R_{\mathrm{T}}\cdot\nabla S$$
$$- \rho(1-f_1)\min\left[C_{2,k\text{-}\varepsilon}R_{\mathrm{T}}^2\left(\frac{\nabla S\cdot\nabla S}{S^2}\right),\ C_m \nabla R_{\mathrm{T}}\cdot\nabla R_{\mathrm{T}}\right] + \lambda_{R_{\mathrm{T}}} f_{r,v}(\alpha) R_{\mathrm{T}}. \tag{4}$$

Here, $\boldsymbol{v}$ is the mean fluid velocity, p is the mean fluid (static) pressure, T_{K} is the mean fluid absolute temperature, $\rho = \rho(p, T_{\mathrm{K}}) = \frac{pM_{molar}}{R_U T_{\mathrm{K}}}$ is the ideal gas model density (M_{molar} is the molar mass of the gas, and R_U is the universal gas constant (8.314 J/(K mol))), $e_{\mathrm{total}} = u_{\mathrm{int}} + \frac{\boldsymbol{v}\cdot\boldsymbol{v}}{2}$ is the fluid total energy, $u_{\mathrm{int}} = \frac{p}{(\gamma-1)\rho}$ is the fluid internal energy, c_p is the fluid specific heat at constant pressure, c_v is the fluid specific heat at constant volume (for an ideal gas, $c_v = c_p - \frac{R_U}{M_{molar}}$), $\gamma = \frac{c_p}{c_v}$ is the ratio of the fluid specific heats, k_{th} is the fluid thermal conductivity, $\otimes$ is the outer product, $\cdot$ and : are the Euclidean inner products (one- and two-dimensional versions, respectively), $\boldsymbol{f}_r(\alpha)$ is the resistance force used to model the presence of solid material in the design domain (see Section 3), $\mu_{\mathrm{T}} = \mu_{\mathrm{T}}(R_{\mathrm{T}}) = \rho f_\mu R_{\mathrm{T}}$ is the turbulent viscosity, R_{T} is the undamped eddy (turbulent) viscosity, $\lambda_{R_{\mathrm{T}}}$ is an adjustable parameter for the intensity of the attenuation of turbulence inside the modelled solid material (it can be chosen, for example, as $\lambda_{R_{\mathrm{T}}} = 1$), and $f_{r,v}(\alpha)$ is the proportion factor of the resistance force of the porous medium (specified from $\boldsymbol{f}_r(\alpha)$ as $\boldsymbol{f}_r(\alpha) = f_{r,v}(\alpha)\boldsymbol{v}$). The other terms of (4) are specified as follows (Han *et al.*, 2018):

$$\begin{aligned}
&\boldsymbol{S} = \frac{1}{2}(\nabla\boldsymbol{v} + \nabla\boldsymbol{v}^T),\ S = \sqrt{2\boldsymbol{S}{:}\boldsymbol{S}},\ \boldsymbol{W} = \frac{1}{2}(\nabla\boldsymbol{v} - \nabla\boldsymbol{v}^T),\ W = \sqrt{2\boldsymbol{W}{:}\boldsymbol{W}},\\
&f_\mu = \frac{\chi^3}{\chi^3 + c_w^3},\ \chi = \frac{R_{\mathrm{T}}}{\nu},\ c_w = 8.54,\ \eta = S\max\left[1,\ \left|\frac{W}{S}\right|\right],\ C_m = 8.0,\\
&\sigma_R = f_1(\sigma_{k\text{-}\omega} - \sigma_{k\text{-}\varepsilon}) + \sigma_{k\text{-}\varepsilon},\ \sigma_{k\text{-}\varepsilon} = 1,\ \sigma_{k\text{-}\omega} = 0.72,\\
&f_1 = \tanh(\arg_1^4),\ \arg_1 = \frac{\nu + R_{\mathrm{T}}}{2}\frac{\eta^2}{C_\mu\, k_T|_{\text{log-layer}}\ \omega_T|_{\text{log-layer}}},\\
&k_T|_{\text{log-layer}} = \frac{\nu_{\mathrm{T}} S}{\sqrt{C_\mu}},\ \ \omega_T|_{\text{log-layer}} = \frac{S}{\sqrt{C_\mu}},\ C_\mu = 0.09,\\
&C_1 = f_1(C_{1,k\text{-}\omega} - C_{1,k\text{-}\varepsilon}) + C_{1,k\text{-}\varepsilon},\ C_{2,k\text{-}\omega} = \frac{C_{1,k\text{-}\omega}}{\kappa_{vk}^2} + \sigma_{k\text{-}\omega},\ C_{2,k\text{-}\varepsilon} = \frac{C_{1,k\text{-}\varepsilon}}{\kappa_{vk}^2} + \sigma_{k\text{-}\varepsilon},\\
&C_{1,k\text{-}\omega} = 0.0829,\ C_{1,k\text{-}\varepsilon} = 0.1284,\ \nu_{\mathrm{T}} = \frac{\mu_{\mathrm{T}}}{\rho},\\
&\kappa_{vk} = 0.41 \text{ (von Kármán constant)},\ \nu = \frac{\mu}{\rho} \text{ (kinematic viscosity)}.
\end{aligned} \tag{5}$$

The fluid stress tensor $\boldsymbol{T}$ and the Reynolds (turbulent) stress tensor $\boldsymbol{T}_R$ are given by:

$$\boldsymbol{T} = 2\mu\boldsymbol{\epsilon} - p\boldsymbol{I} + \lambda(\nabla\cdot\boldsymbol{v})\boldsymbol{I}, \quad \boldsymbol{\epsilon} = \frac{1}{2}(\nabla\boldsymbol{v} + \nabla\boldsymbol{v}^T), \tag{6}$$

$$\boldsymbol{T}_R = 2\mu_{\mathrm{T}}\boldsymbol{\epsilon} + \lambda_{\mathrm{T}}(\nabla\cdot\boldsymbol{v})\boldsymbol{I}, \tag{7}$$

where μ is the dynamic viscosity of the fluid, $\lambda = -\frac{2}{3}\mu$ is the dilatational viscosity of the fluid, $\boldsymbol{I}$ is the identity matrix and μ_{T} is the turbulent viscosity. As in the case of the dilatational viscosity (λ), the turbulent counterpart (λ_{T}) is also be given in the same way. The turbulent thermal conductivity from (3) is given by:

$$k_{th,\mathrm{T}} = \frac{c_p \mu_{\mathrm{T}}}{\mathrm{Pr}_{\mathrm{T}}}, \tag{8}$$

where Pr_{T} is the turbulent Prandtl number. The turbulent Prandtl number depends on the distance with respect to the walls (Chikh and Campo, 2005; Wilcox, 2006). However, the most common approach in computational fluid dynamics (CFD) is to assume a constant value for it (Wilcox, 2006), such as 0.85, which is the approach taken in this work.

2.1 Discontinuous Galerkin discretisation

To derive the DG discretisation, the equations are multiplied by the test functions on each cell and integrated by parts. Summing over all cells yields jump and average terms on internal facets (Hartmann, 2006; Landet *et al.*, 2020). Separating the convective, dissipative, and other terms and stacking them (Houston and Sime, 2018; Hoellinger *et al.*, 2025), we write the equations as

$$\nabla\cdot\boldsymbol{F}_c(\boldsymbol{u}) = \nabla\cdot\boldsymbol{F}_d(\boldsymbol{u}, \nabla\boldsymbol{u}) + \boldsymbol{F}_e(\boldsymbol{u}), \tag{9}$$

where the convective, dissipative, and other parts are given by

$$\boldsymbol{F}_c(\boldsymbol{u}) = \begin{bmatrix} \rho\boldsymbol{v} \\ p\boldsymbol{I} + (\rho\boldsymbol{v}) \otimes \boldsymbol{v} \\ \rho e_{\text{total}}\boldsymbol{v} + (p\boldsymbol{I})\boldsymbol{v} \\ \rho\boldsymbol{v}R_{\text{T}} \end{bmatrix}, \tag{10}$$

$$\boldsymbol{F}_d(\boldsymbol{u}, \nabla\boldsymbol{u}) = \begin{bmatrix} \boldsymbol{0} \\ (\mu + \mu_{\text{T}})(\nabla\boldsymbol{v} + \nabla\boldsymbol{v}^T) + (\lambda + \lambda_{\text{T}})\text{tr}(\nabla\boldsymbol{v})\boldsymbol{I} \\ (k_{th} + k_{th,\text{T}})\nabla T_{\text{K}} + [(\mu + \mu_{\text{T}})(\nabla\boldsymbol{v} + \nabla\boldsymbol{v}^T) + (\lambda + \lambda_{\text{T}})\text{tr}(\nabla\boldsymbol{v})\boldsymbol{I}]\boldsymbol{v} \\ (\sigma_R\rho R_{\text{T}} + \mu)\nabla R_{\text{T}} \end{bmatrix}, \tag{11}$$

$$\boldsymbol{F}_e(\boldsymbol{u}) = \begin{bmatrix} -\frac{\partial\rho}{\partial t} \\ -\frac{\partial(\rho\boldsymbol{v})}{\partial t} + \boldsymbol{f}_r(\alpha) \\ -\frac{\partial(\rho e_{\text{total}})}{\partial t} \\ -\frac{\partial(\rho R_{\text{T}})}{\partial t} + \rho C_1 R_{\text{T}} S + f_1 C_{1,k\text{-}\omega}\rho\frac{R_{\text{T}}}{S}\nabla R_{\text{T}}\cdot\nabla S \\ -\rho(1-f_1)\min\left[C_{2,k\text{-}\varepsilon}R_{\text{T}}^2\left(\frac{\nabla S\cdot\nabla S}{S^2}\right),\ C_m\nabla R_{\text{T}}\cdot\nabla R_{\text{T}}\right] - \lambda_{R_{\text{T}}} f_{r,v}(\alpha)R_{\text{T}} \end{bmatrix}, \tag{12}$$

respectively, where tr is the matrix trace ($\text{tr}(\nabla\boldsymbol{v}) = \nabla\cdot\boldsymbol{v}$), $\boldsymbol{u} = \left[p, \boldsymbol{v}, T_{\text{K}}, R_{\text{T}}\right]^T$ is the state vector, and $\nabla\boldsymbol{u} = \left[\nabla p, \nabla\boldsymbol{v}, \nabla T_{\text{K}}, \nabla R_{\text{T}}\right]^T$ is the gradient of the state vector. Note that eq. (9) is here presented in an extremely generic way, with all specificities condensed in eqs. (10)–(12), where the turbulence terms and equation (from the UFANS formulation) become apparent. Also hidden in the generic notation is the turbulence variable R_{T}, which plays a significant aspect in the definition of the state vector $\boldsymbol{u}$. This configures the major shift from a previous topology optimisation formulation that was based on the much simpler laminar physics (Alonso *et al.*, 2025), and enables considering more realistic fluid properties (such as air), instead of the fictitious/unrealistic fluid properties that were previously selected in order to achieve the compressible flow conditions under small velocities (Alonso *et al.*, 2025). By making use of the presented generic notation, the DG discretisation for transient turbulent compressible flow is given by:

$$\begin{aligned}
&-\int_\Omega \boldsymbol{F}_c(\boldsymbol{u}){:}(\nabla\boldsymbol{w})d\Omega + \int_\Omega \boldsymbol{F}_d(\boldsymbol{u}, \nabla\boldsymbol{u}){:}(\nabla\boldsymbol{w})d\Omega - \int_\Omega \boldsymbol{F}_e(\boldsymbol{u})\cdot\boldsymbol{w}d\Omega \\
&+\int_{\Gamma_{\text{int}}} [\langle\boldsymbol{F}_c(\boldsymbol{u})\rangle + \alpha_{\text{LF}}(\boldsymbol{u})[\![\boldsymbol{u}]\!]_{\otimes,\boldsymbol{n}}]{:}[\![\boldsymbol{w}]\!]_{\otimes,\boldsymbol{n}}d\Gamma_{\text{int}} \\
&-\int_{\Gamma_{\text{int}}} [\langle\boldsymbol{F}_d(\boldsymbol{u}, \nabla\boldsymbol{u})\rangle - \boldsymbol{\alpha}_{\text{SIPG}}(\boldsymbol{u})[\![\boldsymbol{u}]\!]_{\otimes,\boldsymbol{n}}]{:}[\![\boldsymbol{w}]\!]_{\otimes,\boldsymbol{n}}d\Gamma_{\text{int}} - \int_{\Gamma_{\text{int}}} \langle\boldsymbol{F}_d(\boldsymbol{u}, \nabla\boldsymbol{w})\rangle{:}[\![\boldsymbol{u}]\!]_{\otimes,\boldsymbol{n}}d\Gamma_{\text{int}} \\
&+\sum_i \int_{\Gamma_{\text{ext},i}} [\boldsymbol{F}_c(\boldsymbol{u}|_{b,i}) + \alpha_{\text{LF},b}(\boldsymbol{u}, \boldsymbol{u}|_{b,i})(\boldsymbol{u} - \boldsymbol{u}|_{b,i})]{:}(\boldsymbol{w}\otimes\boldsymbol{n})d\Gamma_{\text{ext},i} \\
&-\sum_i \int_{\Gamma_{\text{ext},i}} \{\boldsymbol{F}_d(\boldsymbol{u}|_{b,i}, \nabla\boldsymbol{u})|_{N,i} - \boldsymbol{\alpha}_{\text{SIPG},b}(\boldsymbol{u}|_{b,i})[(\boldsymbol{u} - \boldsymbol{u}|_{b,i})\otimes\boldsymbol{n}]\}{:}(\boldsymbol{w}\otimes\boldsymbol{n})d\Gamma_{\text{ext},i} \\
&-\sum_i \int_{\Gamma_{\text{ext},i}} \boldsymbol{F}_d(\boldsymbol{u}|_{b,i}, \nabla\boldsymbol{w})|_{N,i}{:}[(\boldsymbol{u} - \boldsymbol{u}|_{b,i})\otimes\boldsymbol{n}]d\Gamma_{\text{ext},i} = 0,
\end{aligned} \tag{13}$$

where $\sum_i$ is the sum over all boundaries of the domain, Ω is the computational domain, Γ_{int} are the internal boundaries of each element, $\Gamma_{\text{ext},i}$ is the external boundary of the domain labeled i, $\boldsymbol{n}$ is the unit normal vector over a given facet of the element, $\boldsymbol{w} = \left[w_p, \boldsymbol{w}_v, w_{T_{\text{K}}}, w_{R_{\text{T}}}\right]^T$ is the vector of test functions, $\nabla\boldsymbol{w} = \left[\nabla w_p, \nabla\boldsymbol{w}_v, \nabla w_{T_{\text{K}}}, \nabla w_{R_{\text{T}}}\right]^T$ is the gradient of the vector of test functions, $|_{b,i}$ means to substitute the boundary value (from the Dirichlet boundary condition), $|_{N,i}$ means to substitute the boundary value (from the Neumann boundary condition), the DG tensor jump operator (over $\boldsymbol{u}$) is $[\![\boldsymbol{u}]\!]_{\otimes,\boldsymbol{n}} = (\boldsymbol{u}^+ - \boldsymbol{u}^-)\otimes\boldsymbol{n}$, and the DG average operator (over $\boldsymbol{u}$) is $\langle\boldsymbol{u}\rangle = \frac{1}{2}(\boldsymbol{u}^+ + \boldsymbol{u}^-)$. The superscripts "+" and "-" represent the values of the variable as viewed by the current element, and as viewed by the neighbour element, respectively. The divergence operator in eq. (9) is defined as $\nabla\cdot\boldsymbol{F} = \left[\nabla\cdot\boldsymbol{F_1}, \nabla\cdot\boldsymbol{F_2}, \nabla\cdot\boldsymbol{F_3}, \nabla\cdot\boldsymbol{F_4}\right]^T$, when considering a generic stacked term $\boldsymbol{F} = \left[\boldsymbol{F_1}, \boldsymbol{F_2}, \boldsymbol{F_3}, \boldsymbol{F_4}\right]^T$.

The second and fourth lines of (13) correspond to the convective numerical flux according to the local Lax–Friedrichs scheme (aka. Rusanov scheme) (Cockburn and Shu, 2001; Gassner and Winters, 2021), which includes an additional diffusivity in the equations, by means of a locally-selected weight. The parameter $\alpha_{\mathrm{LF}}(\boldsymbol{u})$ is a measure of the propagation speed on the facets, meaning that it is a local dissipation. The parameter $\alpha_{\mathrm{LF},b}(\boldsymbol{u},\boldsymbol{u}|_{b,i})$ is the corresponding value of $\alpha_{\mathrm{LF}}(\boldsymbol{u})$ for the boundaries. These two parameters are given as:

$$\begin{aligned}\alpha_{\mathrm{LF}}(\boldsymbol{u}) &= \frac{1}{2}\max(\max_i|\lambda_{e,i}(\boldsymbol{u})^+|,\max_i|\lambda_{e,i}(\boldsymbol{u})^-|),\\ \alpha_{\mathrm{LF},b}(\boldsymbol{u},\boldsymbol{u}|_{b,i}) &= \frac{1}{2}\max(\max_i|\lambda_{e,i}(\boldsymbol{u})|,\max_i|\lambda_{e,i}(\boldsymbol{u}|_{b,i})|),\end{aligned} \tag{14}$$

where $\lambda_{e,i}$ is one of the eigenvalues of the convective part (Rohde, 2001)—for compressible flow, it is $\boldsymbol{\lambda}_e(\boldsymbol{u}) = \left[\boldsymbol{v}\cdot\boldsymbol{n}-c, \boldsymbol{v}\cdot\boldsymbol{n}, \boldsymbol{v}\cdot\boldsymbol{n}+c,\right]^T$, where $c=\sqrt{\frac{\gamma p}{\rho}}$ is the speed of sound. Note that, although the overall DG formulation is here presented in a generic way, the choice of these eigenvalues is the only aspect that is the same as Alonso *et al.*, (2025), since the other terms depend on $\boldsymbol{u}$, which depends on turbulence.

Eq. (13) uses the Symmetric Interior Penalty Galerkin (SIPG) formulation (Hartmann and Houston, 2008), which means that additional penalty terms are applied to the dissipative part of the problem. These are the terms that include $\boldsymbol{\alpha}_{\mathrm{SIPG}}(\boldsymbol{u})$ and $\boldsymbol{\alpha}_{\mathrm{SIPG},b}(\boldsymbol{u}|_{b,i})$. With this, SIPG essentially deals the imposition of Dirichlet boundary conditions and additional stabilisations in the equations. The terms $\boldsymbol{\alpha}_{\mathrm{SIPG}}(\boldsymbol{u})$ and $\boldsymbol{\alpha}_{\mathrm{SIPG},b}(\boldsymbol{u}|_{b,i})$ are given by

$$\begin{aligned}\boldsymbol{\alpha}_{\mathrm{SIPG}}(\boldsymbol{u}) &= c_{ip}\frac{p_{\mathrm{DG}}^2}{\min(h^+,h^-)}\langle\boldsymbol{G}(\boldsymbol{u})\rangle,\\ \boldsymbol{\alpha}_{\mathrm{SIPG},b}(\boldsymbol{u}|_{b,i}) &= c_{ip}\frac{p_{\mathrm{DG}}^2}{h}\boldsymbol{G}(\boldsymbol{u}|_{b,i}),\end{aligned} \tag{15}$$

where $h=\frac{V_{\mathrm{local}}}{A_{\mathrm{facet}}}$ is a measure of the element size in the mesh (V_{local} is the volume of each element, and A_{facet} is the area of each facet), $p_{\mathrm{DG}} \geqslant 1$ is the degree of the DG element, $c_{ip} > 0$ is the interior penalty parameter (which needs be chosen to be sufficiently large), and $\boldsymbol{G}(\boldsymbol{u}) = \frac{\partial \boldsymbol{F}_d}{\partial \boldsymbol{u}}$ is the homogeneity tensor.

2.2 *Boundary value problem*

The external boundaries of a sample computational domain are shown in Fig. 1. With respect to a previously considered laminar flow-based formulation (Alonso *et al.*, 2025), there are now turbulence terms and an additional equation for them (from the UFANS formulation) and the boundary conditions now also need to be defined for the turbulence variable R_{T}. Thus, the boundary value problem is stated as:

$$\begin{aligned}[\text{Eqs. (1)-(4)}] \quad &\text{in } \Omega\\ \boldsymbol{v} = \boldsymbol{v}_{in} \quad &\text{on } \Gamma_{\mathrm{in}}\\ T_{\mathrm{K}} = T_{\mathrm{K},in} \quad &\text{on } \Gamma_{\mathrm{in}}\\ R_{\mathrm{T}} = R_{\mathrm{T},in} \quad &\text{on } \Gamma_{\mathrm{in}}\\ \boldsymbol{v} = \boldsymbol{0} \quad &\text{on } \Gamma_{\mathrm{wall}}\\ \nabla T_{\mathrm{K}}\cdot\boldsymbol{n} = 0 \quad &\text{on } \Gamma_{\mathrm{wall}}\\ R_{\mathrm{T}} = 0 \quad &\text{on } \Gamma_{\mathrm{wall}}\\ p = p_{out} \quad &\text{on } \Gamma_{\mathrm{out}}\\ \nabla T_{\mathrm{K}}\cdot\boldsymbol{n} = 0 \quad &\text{on } \Gamma_{\mathrm{out}}\\ \nabla R_{\mathrm{T}}\cdot\boldsymbol{n} = 0 \quad &\text{on } \Gamma_{\mathrm{out}},\end{aligned} \tag{16}$$

where the inlet boundary is Γ_{in}, the outlet boundary is Γ_{out}, the wall boundaries are Γ_{wall}, the inlet velocity is $\boldsymbol{v}_{in}$, the inlet temperature is $T_{\mathrm{K},in}$, the inlet turbulence is set from $R_{\mathrm{T},in}$, and the outlet (static) pressure is p_{out}. The walls are treated as adiabatic, and the outlet is set for the normal turbulence and heat fluxes to be zero. The Dirichlet conditions in (16) are enforced weakly with a standard Nitsche approach.

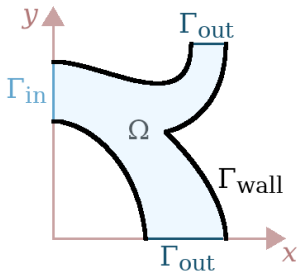

Figure 1: Boundaries (Source: Authors own work).

3 Topology optimisation formulation

The topology optimisation formulation is further detailed as follows, by presenting the material model, which guides how the design variable affects the simulation/optimisation, and the overall formulation of the topology optimisation problem, including the presentation of the objective functions and constraints.

3.1 Material model

The material model for fluid flow influences three main components: the fluid flow itself, the heat transfer/compressibility, and the turbulence. For the first component, the modelled solid material should not have any flow inside—this motivates the additional resistance force $\boldsymbol{f}_r(\alpha)$ employed. For the second component, the modelled solid material zones are assumed to be adiabatic, thus no additional term needs to be included in the energy equation (Sá *et al.*, 2021). For the third component, the wall value is set as zero inside the modelled solid material, from the $f_{r,v}(\alpha)$ term. The resistance force $\boldsymbol{f}_r(\alpha)$ is given by:

$$\boldsymbol{f}_r(\alpha) = -\kappa(\alpha)\boldsymbol{v}, \tag{17}$$

where $\kappa(\alpha)$ is the inverse permeability.

The interpolation function that is used for $\kappa(\alpha)$ to smoothly transition between the solid ($\alpha = 0$) and fluid ($\alpha = 1$) conditions is (Borrvall and Petersson, 2003):

$$\kappa(\alpha) = \kappa_{\max} + (\kappa_{\min} - \kappa_{\max})\alpha\frac{1+q}{\alpha+q}, \tag{18}$$

where $\kappa_{\min} = 0$ kg/(m^{3}s) and $\kappa_{\max}$ are the minimum and maximum values for it, respectively; and q is a penalisation parameter.

3.2 Topology optimisation problem

The topology optimisation problem is:

$$\boxed{\begin{aligned}&\min_{\alpha}\ J(\boldsymbol{u}(\alpha),\alpha)\\&\textbf{such that}\\&\quad\text{Fluid volume constraint: } \int_{\Omega_\alpha}\alpha d\Omega_\alpha \leqslant fV_0\\&\quad\text{Box constraint of } \alpha\text{: } 0 \leqslant \alpha \leqslant 1\end{aligned}}, \tag{19}$$

where f is the specified volume fraction, $V_0 = \int_{\Omega_\alpha} d\Omega_\alpha$ is the volume of the design domain (represented as Ω_α), $V = \int_{\Omega_\alpha}\alpha d\Omega_\alpha$ is the fluid volume given from the design variable α, $J(\boldsymbol{u}(\alpha),\alpha)$ is the objective function, and $\boldsymbol{u}(\alpha)$ is the state vector obtained by solving the boundary value problem (16) for a given design variable α.

For topology optimisation, more than one type of objective function is considered, and, for the sake of clarity, the specific objective functions being considered are presented in each numerical example. When there is more than one objective function being considered, the objective functions are combined through the logarithmic approach:

$$J = \sum_i a_i w_i \ln J_i, \tag{20}$$

where J_i is an objective function, w_i is its weight ($w_i \geqslant 0$), a_i indicates whether J_i is to be minimised ($a_i = 1$) or maximised ($a_i = -1$), and ln is the natural logarithm.

3.2.1 Transient topology optimisation approach

For optimisation, two types of objective function are considered.
We first consider energy dissipation (Borrvall and Petersson, 2003). For transient turbulent compressible flow, it becomes the following time average:

$$\Phi_t = \frac{1}{t_f - t_0} \int_{t_0}^{t_f} \left\{ \int_\Omega \left[\frac{1}{2}(\mu + \mu_\mathrm{T})(\nabla \boldsymbol{v} + \nabla \boldsymbol{v}^T) : (\nabla \boldsymbol{v} + \nabla \boldsymbol{v}^T) \right] d\Omega + \int_\Omega (\lambda + \lambda_\mathrm{T})(\nabla \cdot \boldsymbol{v})(\boldsymbol{I} : \nabla \boldsymbol{v}) d\Omega - \int_\Omega \boldsymbol{f}_r(\alpha) \cdot \boldsymbol{v} d\Omega \right\} dt, \tag{21}$$

where the integration is given in the time interval $[t_0, t_f]$, where t_0 is the initial time of the unsteady simulation, and t_f is the final time of the unsteady simulation.

Second, we consider mass flow rate. When there is more than one outlet in the fluid flow device, we may want a configuration in which one of the available outlets is prioritised with respect to the others, with the preferred outlet depending on the inlet flow rate value. This is the behaviour desired of fluid switches. In such case, the mass flow rate can be used as an objective function. It is given by:

$$\dot{m}_{t,1' \to 2',i} = \frac{1}{t_{2'} - t_{1'}} \int_{t_{1'}}^{t_{2'}} \left(\int_{\Gamma_i} \rho \boldsymbol{v} \cdot \boldsymbol{n} d\Gamma_i \right) dt, \tag{22}$$

where the integration is given in the time interval $[t_{1'}, t_{2'}]$, on the outlet boundary Γ_i.

3.2.2 Multi-objective steady-state topology optimisation approach

When considering a transient behaviour composed of two different values of the flow rate, together with a transition between these two values, it is possible to devise a multi-objective steady-state approach that is similar to the transient formulation. This multi-objective steady-state approach would consider the two flow rate cases simultaneously, for each flow rate value. Of course, this steady-state formulation is unable to consider the transient behaviour caused by the change in the flow rate. This will be shown in one of the numerical examples. The multi-objective steady-state approach consists of considering two different steady-state cases under different flow rates, which are labeled here as "1" and "2". Thus, the energy dissipation (21) becomes two separated objective functions:

$$\Phi(\boldsymbol{u}_1) = \int_\Omega \left[\frac{1}{2}(\mu + \mu_{\mathrm{T},1})(\nabla \boldsymbol{v}_1 + \nabla \boldsymbol{v}_1{}^T) : (\nabla \boldsymbol{v}_1 + \nabla \boldsymbol{v}_1{}^T) \right] d\Omega + \int_\Omega (\lambda + \lambda_{\mathrm{T},1})(\nabla \cdot \boldsymbol{v}_1)(\boldsymbol{I} : \nabla \boldsymbol{v}_1) d\Omega - \int_\Omega \boldsymbol{f}_r(\alpha) \cdot \boldsymbol{v}_1 d\Omega, \tag{23}$$

$$\Phi(\boldsymbol{u}_2) = \int_\Omega \left[\frac{1}{2}(\mu + \mu_{\mathrm{T},2})(\nabla \boldsymbol{v}_2 + \nabla \boldsymbol{v}_2{}^T) : (\nabla \boldsymbol{v}_2 + \nabla \boldsymbol{v}_2{}^T) \right] d\Omega + \int_\Omega (\lambda + \lambda_{\mathrm{T},2})(\nabla \cdot \boldsymbol{v}_2)(\boldsymbol{I} : \nabla \boldsymbol{v}_2) d\Omega - \int_\Omega \boldsymbol{f}_r(\alpha) \cdot \boldsymbol{v}_2 d\Omega, \tag{24}$$

where the subindices "1" and "2" indicate the steady-state case in which the computation is performed.

The mass flow rate objective function would become:

$$\dot{m}(\boldsymbol{u}_j) = \int_{\Gamma_i} \rho \boldsymbol{v}_j \cdot \boldsymbol{n} d\Gamma_i, \tag{25}$$

where j is the subindex that indicate the steady-state case in which the computation is performed.

4 Numerical implementation of the topology optimisation problem

The topology optimisation problem is implemented according to Fig. 2. The beginning is to select an initial guess for the distribution of the design variable – i.e., set the initial topology. Then, the forward model is defined in two steps: first, the convective, dissipative and external terms (10)–(12) are defined in the finite element-based platform FEniCS (Logg *et al.*, 2012), by using DG1 (1st degree Discontinuous Galerkin) discretisation for the state variables, and CG1 (1st degree Continuous Galerkin) discretisation for the design variable (in order to guarantee continuity of the optimised topologies); next, these terms are set in the `dolfin_dg` library (Houston and Sime, 2018) in order to automatically assemble eq. (13). While it is possible to implement the DG discretisation

directly in FEniCS, using it is more convenient in the sense that it allows further flexibility when changing the involved physics and boundary conditions of the problem. The defined forward model is then annotated for later derivation of the adjoint model using the dolfin-adjoint library (Farrell *et al.*, 2013; Mitusch *et al.*, 2019). The next part is the Topology Optimisation of Binary Structures (TOBS) algorithm (Souza *et al.*, 2021; Sivapuram and Picelli, 2018), which is based on binary variables, uses the derivatives of the DG problem, and linearises the optimisation problem at every topology optimisation iteration. Also, the constraints are relaxed, and an additional truncation error constraint is included. The resulting topology optimisation subproblem is then solved in CPLEX® (from IBM). A specified tolerance is verified in the end of the topology optimisation loop.

In the case of turbulent and high velocity flows, there may be some difficulties in the convergence of the forward problem in FEniCS, which can most probably be dealt with by including various adjustments, such as: preconditioners, block matrices, additional limiters, approximated terms, continuations, different solution methods etc. However, the choice and implementations are neither easy nor trivial, due to which another approach is followed here, which is to interface with a well-established efficient CFD platform, OpenFOAM® (Weller *et al.*, 1998). In OpenFOAM® , the density-based `rhoCentralFoam` solver is employed, including some additional adjustments: including the material model terms, and considering the classic fourth-order Runge–Kutta method (RK4) for the time discretisation. The time step is left for OpenFOAM® to select according to the Courant–Friedrichs–Lewy (CFL) condition, by setting a maximum value of 0.2 for it. In steady-state simulations, the `rhoSimpleFoam` solver is considered similarly.

The main drawback with OpenFOAM® is its lack of an adjoint model. We therefore employ FEniCS/dolfin-adjoint for the adjoint calculations. The two models use different discretisations in space, and also in time (implicit Euler for the adjoint). Numerical time integration of the objective functions is performed with the trapezoidal rule. The interaction between FEniCS/dolfin-adjoint and OpenFOAM® is implemented by following the same approach from Alonso *et al.*, (2021), by substituting only the `solve` function from FEniCS/dolfin-adjoint, and using the simulation results from OpenFOAM® . Note that here the conversion between OpenFOAM and FEniCS goes through an initial projection to a continuous (CG1) variable before projecting to the discontinuous (DG1) variable – this is necessary for the computed values to recover variations between neighbouring elements, which would not be possible in a direct projection to DG1. The simulation from OpenFOAM® is computed first, with all timesteps saved to disk, and then they are loaded when FEniCS/dolfin-adjoint require them. The different discretisations mean that the gradients computed are not discretely consistent; however, the physical problem is still the same, and the presented approach gives descent directions for the topology optimisation in all cases tested. The numerical examples also consider a sensitivity filter based on the modified Helmholtz equation (Lazarov and Sigmund, 2010). Furthermore, aiming to reduce mesh-dependency effects in the sensitivities, we scale the sensitivities by an L^2 Riesz map (Schwedes *et al.*, 2017).

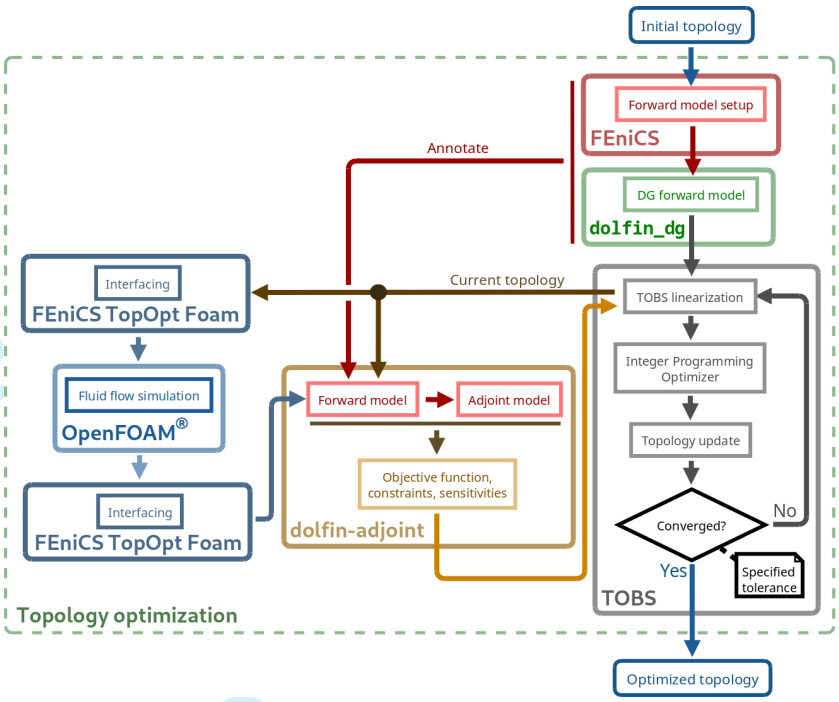

Figure 2: Flowchart of the topology optimisation implementation (Source: Authors own work).

5 Numerical results

For the numerical experiments we consider air (c_p = 1004 J/(kg K), $\mu = 18.37\times10^{-6}$ Pa s, $k_{th} = 26.3\times10^{-3}$ W/(m K), and M_{molar} = 28.96 g/mol). The boundary conditions are guided by $T_{\mathrm{K},in}$ = 298.15 K and $p_{out} = 10^5$ Pa. Transient effects are induced by changing the inlet flow rate, while the initial state (at t_0) is set as the steady state simulation of the t_0 configuration. Since the flow is turbulent, the inlet velocity profile $\boldsymbol{v}_{in}$ is turbulent as well and is set according to De Chant (2005), which is overall similar to the classic $1/7^{\mathrm{th}}$ power law velocity profile (Munson *et al.*, 2009).

The TOBS algorithm is computed until $\Delta\alpha = 0$, or there is a slight loop in the topology (that is, the topology is changing a little bit back and forth; however, is overall converged). The Helmholtz filter radii are set as 0.2807 mm, 0.5394 mm, and 0.2853 mm (changed in the end to 0.42795 mm), respectively, for three numerical examples. The maximum inverse permeability values ($\kappa_{\max}$) are set as $1.0 \sim 2.5 \times 10^{13}\mu$, $2.5 \times 10^{10}\mu$ and $2.5 \times 10^{9}\mu$, for three numerical examples, and the penalisation parameter is set to $q = 1$. The interior penalty parameter is set to $c_{ip} = 10^3$. The parameters of the TOBS algorithm (Souza *et al.*, 2021; Sivapuram and Picelli, 2018) are set as follows, for each numerical example: 0.0001, 0.01 and 0.1, respectively (for $\varepsilon_{\mathrm{relax}}$); 0.005, 0.01 and 0.05, respectively (for $\beta_{\mathrm{flip\ limit}}$). In the third numerical example, continuation was performed, changing to $\varepsilon_{\mathrm{relax}} = 1.0\times10^{-10}$ and $\beta_{\mathrm{flip\ limit}} = 1.0\times10^{-9}$ in the end. The algorithm is computed until the design variable stops changing. The specified maximum fluid volume fractions (f) are set as 30%, 70% and 70%, respectively, for the numerical examples. From the optimised topologies, it is possible to identify the contours of the fluid part of the design domain, which are then considered as shown in Fig. 3, being used to compute the objective function values after the topology optimisation is finished.

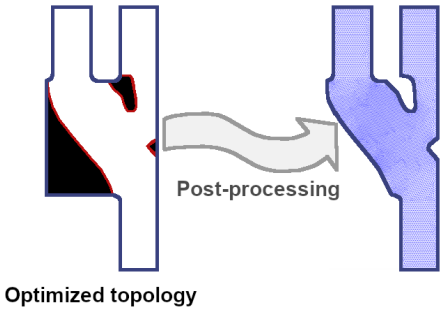

Figure 3: Post-processing procedure (Source: Authors own work).

The inlet turbulent variable ($R_{\mathrm{T},in}$) is given as:

$$R_{\mathrm{T},in} = \sqrt{\frac{n_v}{2}} I_T \ell_T |\boldsymbol{v}_{in}|, \tag{26}$$

where I_T is the turbulence intensity (set as 5%), ℓ_T is the turbulence length scale, $|\boldsymbol{v}_{in}|$ is the local velocity on the inlet, and n_v is the number of velocity components (in 2D, 2 components). Also, ℓ_T is selected as $\ell_T = 0.07 C_\mu^{1/4} \ell_{\mathrm{in}}$ (COMSOL, 2018; CFD Online, 2020) where ℓ_{in} is the size of the inlet.

The Reynolds number is defined as the maximum value of the local Reynolds number based on the size of the inlet:

$$\mathrm{Re}_\ell = \frac{\mu \, |\boldsymbol{v}| \, \ell_{\mathrm{in}}}{\rho}. \tag{27}$$

The characterisation of the fluid flow as compressible depends on the Mach number, which is given as:

$$\mathrm{Ma}_\ell = \frac{|\boldsymbol{v}|}{v_s}, \tag{28}$$

where $v_s = \sqrt{\gamma \frac{R_U}{M_{molar}} T_K}$ is the speed of sound in the fluid.

The time values in the numerical results are represented as the reduced values t', where $t' \in [0.0, 1.0]$. The original time values t can be recovered through the following relation:

$$t = t_0 + (t_f - t_0) t'. \tag{29}$$

Three numerical examples are presented, for a U-bend, a pipe joint, and a double pipe joint. These numerical examples focus on channel-type cases. We focus on these examples because turbomachinery (such as gas turbines) have interconnecting pipes and junctions, which should preferably lead to low energy losses, since they are related to viscous losses, thermal losses and to entropy variation. The first numerical example (U-bend) shows a comparison between the developed transient turbulent compressible flow topology optimisation with a multi-objective steady-state approach only for comparison purposes. The other numerical examples (pipe joint, and double pipe joint) show some further applications of the developed transient turbulent compressible flow topology optimisation. In all cases, the flow is genuinely compressible, which can be seen from the maximum local Mach numbers of about 0.4, 0.6 and 0.4, respectively. The maximum local Reynolds numbers are about $2{\times}10^4$, $1{\times}10^5$ and $3.5{\times}10^4$, respectively, which indicate turbulent conditions.

5.1 U-bend

The first numerical example is a U-bend configuration, which is illustrated in Fig. 4. It is essentially a configuration in which the fluid flow has to perform a U-turn in order to reach the outlet, partially based on Dilgen *et al.*, (2018) (aside from dimensional differences, the inlet/outlet channels are not drawn with modelled solid zones, there is an additional rounding around corners, and the boundary conditions and overall topology optimisation formulation are different). The transient effects are caused by a decrease in the inlet velocity, which is represented by the maximum values for the velocity profile, from $v_{in,\max,0}$ to $v_{in,\max,1}$. The mesh is shown in Fig. 5, being composed of 16,917 elements. A single objective function is considered for minimisation in the transient case: $J = \Phi_t$. When considering the multi-objective steady-state case, the transient objective function Φ_t is split into two: $\Phi(\boldsymbol{u}_1)$ and $\Phi(\boldsymbol{u}_2)$, where $\boldsymbol{u}_1$ and $\boldsymbol{u}_2$ correspond to the steady-state simulations where the velocity profiles are given by $v_{in,\max,0}$, and $v_{in,\max,1}$, respectively. Then eq. (20) is used

to combine both objectives, with $w_1 = w_2 = 1$ (unit weights) and $a_1 = a_2 = 1$ (minimisation). A convergence evaluation for the U-bend configuration is presented in Appendix A.

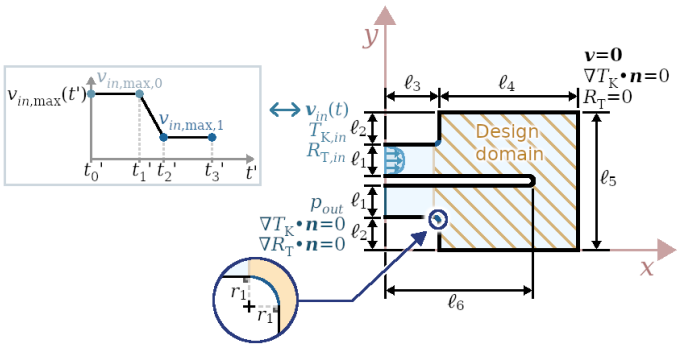

Figure 4: U-bend configuration ($\ell_1 = 2$ mm, $\ell_2 = 2.5$ mm, $\ell_3 = 4$ mm, $\ell_4 = 10$ mm, $\ell_5 = 10$ mm, $\ell_6 = 11$ mm, $r_1 = 0.5$ mm, $v_{in,\max,0} = 60.2$ m/s, $v_{in,\max,1} = 6.02$ m/s, $t_0 = 0$ μs, $t_f = 50$ μs, $t_0' = 0$, $t_1' = 0.4$, $t_2' = 0.6$, $t_3' = 1$ (see eq. (29)), time step: $\Delta t = 1$ μs, initial guess (multi-objective steady-state case): *U letter* shape connecting the inlet to the outlet (tangential to the rod), initial guess (transient case): *U letter* shape connecting the inlet to the outlet (tangential to the rod), performing a continuation from the multi-objective steady-state) (Source: Authors own work).

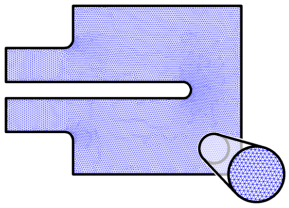

Figure 5: Mesh for the U-bend case (Source: Authors own work).

The topology optimisation results for the transient and multi-objective steady-state cases are shown in Fig. 6, and the objective function values are given in Table I. From Fig. 6, we can notice some curvature differences in the first part of the curve of the optimised topologies, where the transient optimised topology features an initially smaller cross section. This effect can be probably viewed as a way to reduce the turbulence that comes from the sudden decrease in the inlet flow rate, avoiding an initial expansion of the inlet flow. The objective function values from Table I show that the transient optimised topology has a smaller transient energy dissipation Φ_t than the multi-objective steady-state topology, which is expected, since the fluid dynamic behaviours considered in the topology optimisation are different. For the two steady-state values, the results are quite mixed, where the optimised topology for transient flow seems to induce a better value for $\Phi(\boldsymbol{u}_1)$, and a worse value for $\Phi(\boldsymbol{u}_2)$ (with respect to the multi-objective steady-state optimised topology), which might indicate that part of the differences in the optimised topologies might have been induced in the form of a partial contribution of the lower velocity $v_{in,\max,1}$. The convergence curves for the optimised topologies are shown in Fig. 7.

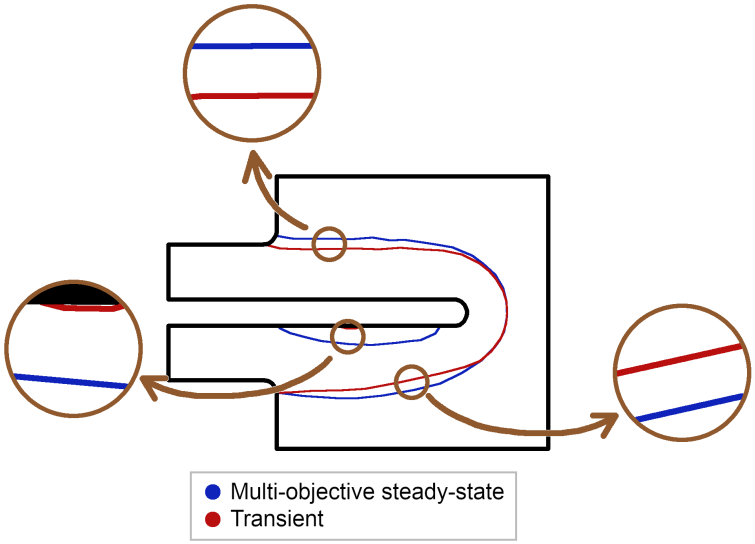

Figure 6: Topology optimisation results for the U-bend case (Source: Authors own work).

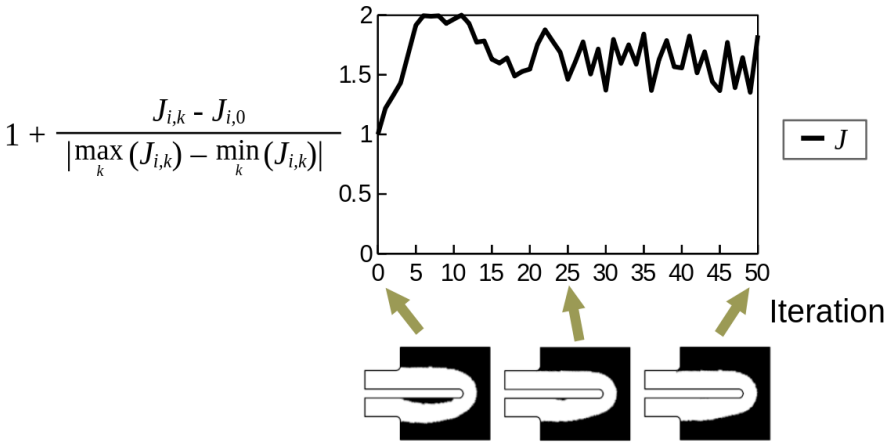

(a) Transient case (Source: Authors own work).

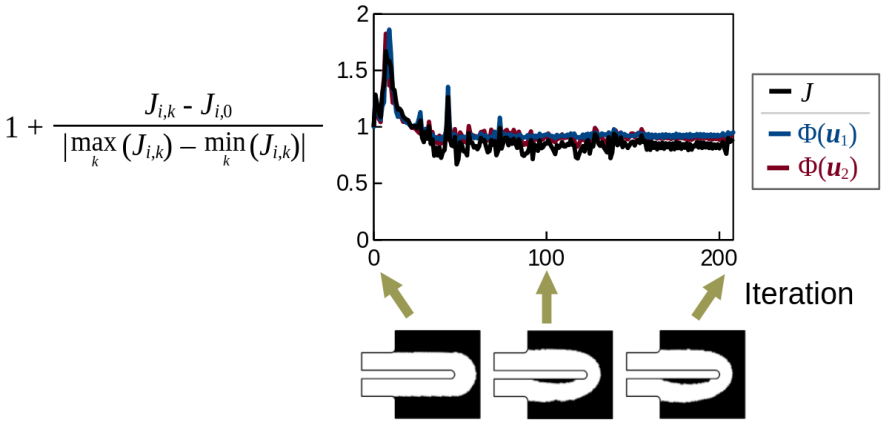

(b) Multi-objective steady-state case (Source: Authors own work).

Figure 7: Convergence curves for the U-bend case (J_i indicates the objective function, and k indicates the number of the iteration).

In order to give a better insight over the two configurations used in the multi-objective steady-state case, the Reynolds number, Mach number and density are shown in Fig. 8. Note that the plots of the Reynolds number indicate that the fluid flow reaches turbulence in both cases (values higher than 10^4). In regards to the Mach number, the first case is compressible, since it features values that are higher than 0.3; however, the second case is not actually compressible, since the

values are consistently smaller than 0.3. As a result, the density values feature a higher variation in the first case (13%), and a small variation in the second case (0.12%).

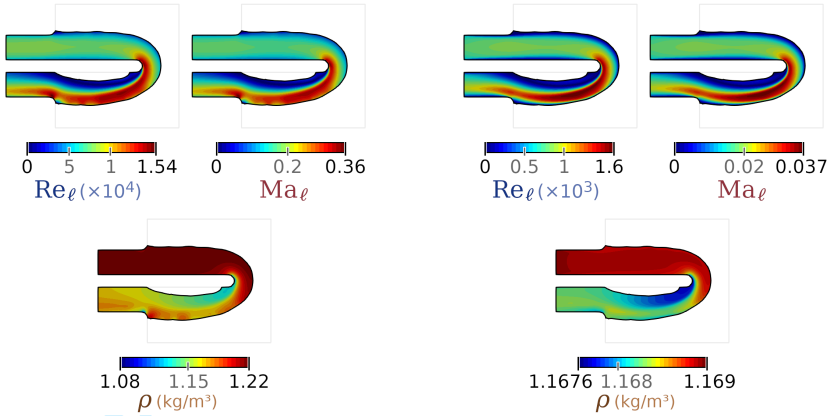

(a) Simulation under $v_{in,\max,0}$ (Source: Authors own work).

(b) Simulation under $v_{in,\max,1}$ (Source: Authors own work).

Figure 8: Steady-state simulations for the multi-objective steady-state U-bend case topology.

The simulation results considering the transient case are shown in Fig. 9. The plots show the velocity, pressure and temperature values. In Fig. 9, we can notice, in $t' = 0.8$ and $t' = 1$, that the smaller velocities caused by $v_{in,\max,0}$ are still propagating towards the outlet, meaning that the fluid flow is still transient at the end. This way, the smaller cross-section at the beginning of the optimised topology seems to be coherent with the small velocities still propagating towards the outlet.

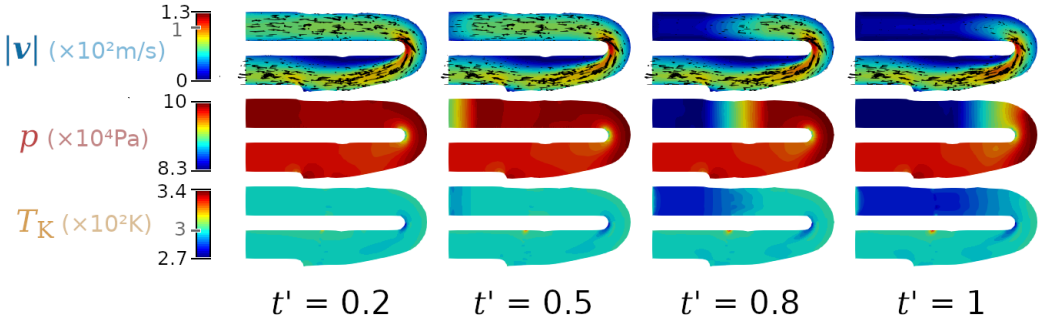

Figure 9: Simulation for the transient U-bend case (Source: Authors own work).

5.2 *Pipe joint*

The second numerical example is a pipe joint configuration, illustrated in Fig. 10. This configuration borrows some inspiration in the positioning of the inlet and outlets from one of the numerical examples from Gersborg-Hansen *et al.*, (2005), which is one of the first works that dealt with the steady-state laminar incompressible Navier–Stokes formulation for topology optimisation. It is essentially a configuration in which the fluid flow has two ways to exit the computational domain: from the upper outlet and from the lower outlet. If left by itself, topology optimisation tends to choose the outlet that would lead to a smaller energy dissipation. Therefore, one aim is to optimise objective functions for both outlets, avoiding any type of closure. Furthermore, the lower outlet is set to be prioritised when the inlet flow rate is higher, and the upper outlet to be prioritised when the inlet flow rate is lower, which resembles the behaviour of fluid switches. The transient effects are caused by a decrease in velocity, which is represented by the maximum values for the velocity profile, from $v_{in,\max,0}$ to $v_{in,\max,1}$. The mesh is shown in Fig. 11, being composed of 12,814 elements. In this case, three objectives are simultaneously considered: minimising the energy dissipation Φ_t, maximising the mass flow rate over the lower outlet in the beginning $\dot{m}_{t,0\to1,\text{Outlet 1}}$ and maximising the mass flow rate over the upper outlet in the end $\dot{m}_{t,2\to3,\text{Outlet 2}}$. Then, eq. (20) is used to combine the three objectives, with $w_1 = w_2 = w_3 = 1$ (unit weights), $a_1 = 1$ (minimisation) and $a_2 = a_3 = -1$ (maximisation).

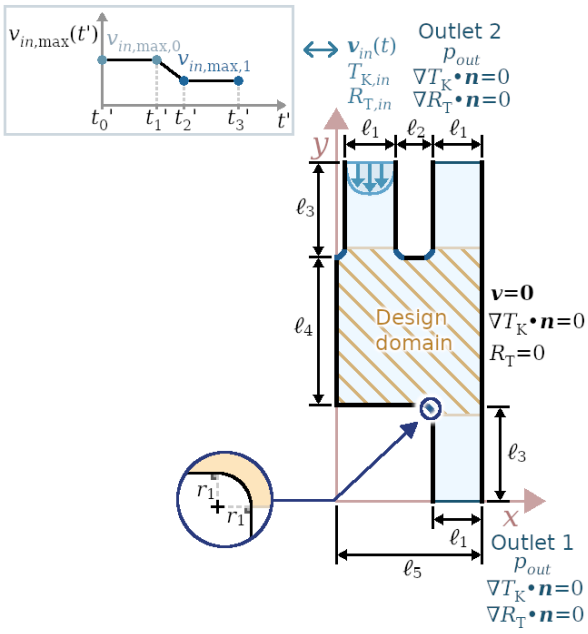

Figure 10: Pipe joint configuration ($\ell_1 = 10$ mm, $\ell_2 = 8$ mm, $\ell_3 = 20$ mm, $\ell_4 = 30$ mm, $r_1 = 2$ mm, $v_{in,\max,0} = 150.4$ m/s, $v_{in,\max,1} = 120.32$ m/s, $t_0 = 0$ μs, $t_f = 50$ μs, $t_0' = 0$, $t_1' = 0.4$, $t_2' = 0.6$, $t_3' = 1$ (see eq. (29)), time step: $\Delta t = 1$ μs, initial guess: $\alpha = 1$) (Source: Authors own work).

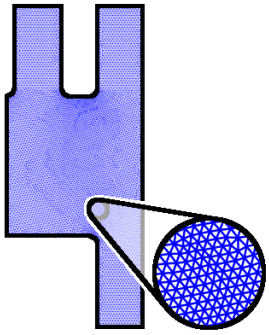

Figure 11: Mesh for the pipe joint case (Source: Authors own work).

The optimised topology is shown in Fig. 12, and the objective function values are given in Table II. Note that the topology optimisation did not close any of the two outlets, keeping a flow passage upwards, while still prioritising the reduction of the energy dissipation downwards. This can also be observed in the values from Table II, where the optimised topology features a lower energy dissipation Φ_t than the fluid case, while somewhat decreasing the mass flow rate downwards $\dot{m}_{t,0\to1,\text{Outlet 1}}$ and slightly increasing the mass flow rate upwards $\dot{m}_{t,2\to3,\text{Outlet 2}}$. This effect is caused by the equal weight being used in the multi-objective function, which brings the upper outlet to a similar influence in the optimisation with respect to the lower outlet. Note that the mass flow rates are different in both cases, which is caused by the different time integration periods of $\dot{m}_{t,0\to1,\text{Outlet 1}}$ and $\dot{m}_{t,2\to3,\text{Outlet 2}}$.

Figure 12: Optimised topology for the pipe joint case (Source: Authors own work).

The simulation results for the optimised topology are shown in Fig. 13. Note that a small portion of the fluid flow exits through the upper outlet. Also, note that, as in the U-bend case, the change to the smaller flow rate is slowly propagating towards the rest of the computational domain.

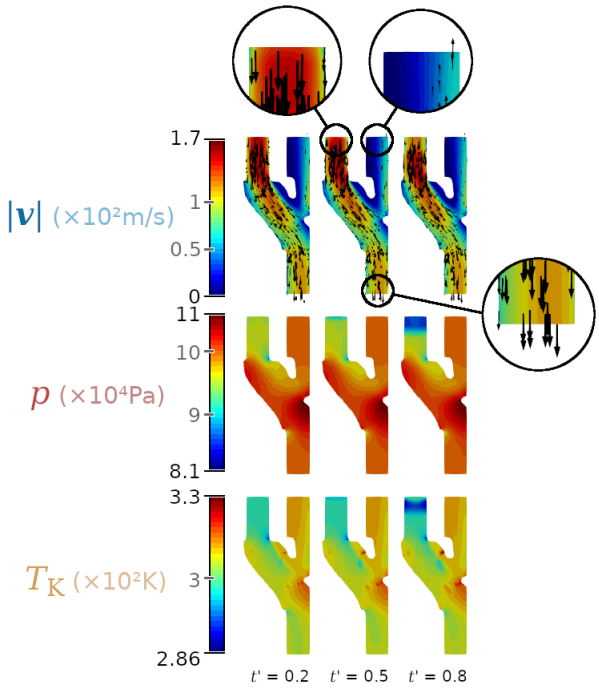

Figure 13: Simulation for the pipe joint case (Source: Authors own work).

5.3 Double pipe joint

The last numerical example is a double pipe joint configuration, illustrated in Fig. 14. In this case, we have two inlets and two outlets, positioned in a crossed configuration. Similarly to the previous numerical example, if left by itself, topology optimisation tends to choose the outlet that would lead to a smaller energy dissipation. Therefore, one aim is to avoid any type of closure. Furthermore, the right outlet is set to be prioritised when the inlet flow rate is higher, and the left outlet to be prioritised when the inlet flow rate is lower. Here, differently than the previous numerical examples, the transient effects are caused by an increase in the inlet velocity, which is represented by the maximum values for the velocity profile, from $v_{in,1,\max,0}$ to $v_{in,1,\max,1}$. The mesh is shown in Fig. 15, being composed of 17,034 elements. In this case, three objectives are simultaneously considered, as in the previous numerical example: minimising the energy dissipation Φ_t, maximising the mass flow rate over the left outlet $\dot{m}_{t,0\to1,\text{Outlet 2}}$ and maximising the mass flow rate over the right outlet $\dot{m}_{t,2\to3,\text{Outlet 1}}$. Then, eq. (20) is used to combine the three objectives, with $w_1 = w_3 = 1$, $w_2 = 10$, $a_1 = 1$ (minimisation) and $a_2 = a_3 = -1$ (maximisation).

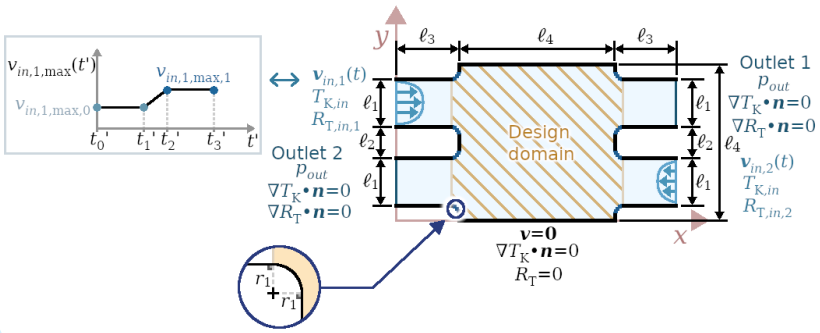

Figure 14: Double pipe joint configuration ($\ell_1 = 3$ mm, $\ell_2 = 2$ mm, $\ell_3 = 4$ mm, $\ell_4 = 10$ mm, $r_1 = 0.5$ mm, $v_{in,1,\max,0} = 11.39$ m/s, $v_{in,1,\max,1} = 113.94$ m/s, $v_{in,2} = 0.1v_{in,1}$, $t_0 = 0$ μs, $t_f = 50$ μs, $t_0' = 0$, $t_1' = 0.4$, $t_2' = 0.6$, $t_3' = 1$ (see eq. (29)), time step: $\Delta t = 1$ μs, initial guess: $\alpha = 1$, performing a continuation from a multi-objective steady-state) (Source: Authors own work).

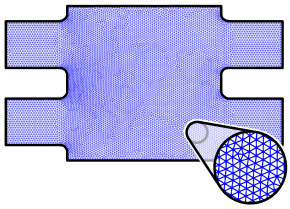

Figure 15: Mesh for the double pipe joint case (Source: Authors own work).

The optimised topology is shown in Fig. 16, and the objective function values are indicated in Table III. Note that, as in the previous numerical example, the topology optimisation did not close any of the two outlets. This can also be observed in the values from Table III, where the optimised topology features a lower energy dissipation Φ_t than the fluid case, while increasing the mass flow rate to the left $\dot{m}_{t,0\to1,\text{Outlet 2}}$ and somewhat decreasing the mass flow rate to the right $\dot{m}_{t,2\to3,\text{Outlet 1}}$. This effect can be noticed in the optimised topology in Fig. 16, where the left inlet is split into two paths (for both outlets), and the right inlet is channeled towards the left outlet.

Figure 16: Optimised topology for the double pipe joint case (Source: Authors own work).

The simulation results for the optimised topology are shown in Fig. 17. Note that the fluid flow that enters through the left inlet is goes towards the left and right inlets, while the fluid flow that enters through the right inlet seems to exit through the left outlet. Also, note that the change to the higher flow rate is still propagating towards the rest of the computational domain; however, due to the transition from a lower velocity to a higher velocity, the transition seems to propagate somewhat faster than in the previous examples. Also, note that the increase in velocity with time caused an increase in the flow velocity near the corners of the left inlet channel.

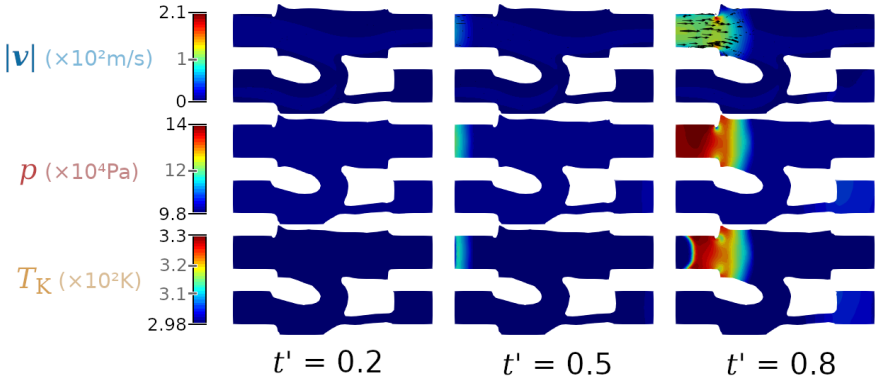

Figure 17: Simulation for the pipe joint case (Source: Authors own work).

6 Conclusions

A new formulation for the topology optimisation of turbulent transient compressible flow was presented, using OpenFOAM® for the forward model and a DG discretisation for the adjoint model. The developed formulation is illustrated with three numerical examples. The proposed approach was compared with a multi-objective steady-state approximation in one of the numerical examples (U-bend), showing that this steady-state approximation is unable to capture transient effects, resulting in reduced performance (according to the objective function values). The other numerical examples were presented to exemplify the unsteady implications. The second numerical example shows a larger flow path downwards and a smaller flow path upwards when prioritising the upwards flow path after the transition to a smaller flow rate. The third numerical example shows that the left inlet has large channels towards both outlets, while the right inlet has a smaller channel, trying to lead the flow solely towards the left outlet. As future work, this work may be extended to fluid-structure interaction, other types of heat transfer, flow machine design, 3D setups, and supersonic flows.

Table I: Objective functions of the optimised topologies for the U-bend case (Source: Authors own work).

Optimised topology	Transient simulation Φ_t ($\times 10^2$W/m)	Steady-state simulations $\Phi(\boldsymbol{u}_1)$ ($\times 10^2$W/m)	$\Phi(\boldsymbol{u}_2)$ ($\times 10^{-1}$W/m)
Transient	1.05	1.37	4.12
Multi-objective steady-state	1.11	2.45	3.34

Table II: Objective functions for the pipe joint case (Source: Authors own work).

Case	Φ_t ($\times 10^3$W/m)	$\dot{m}_{t,0\to1,\text{Outlet 1}}$ ($\times 10^{-1}$kg/s)	$\dot{m}_{t,2\to3,\text{Outlet 2}}$ (kg/s)
Initial guess (fluid, $\alpha = 1$)	1.62	3.6	1.14
Optimised topology	1.19	3.17	1.18

Table III: Objective functions for the double pipe joint case (Source: Authors own work).

Case	Φ_t (W/m)	$\dot{m}_{t,0\to1,\text{Outlet 2}}$ ($\times 10^{-2}$kg/s)	$\dot{m}_{t,2\to3,\text{Outlet 1}}$ ($\times 10^{-2}$kg/s)
Initial guess (fluid, $\alpha = 1$)	6.51	0.95	2.97
Optimised topology	5.52	1.75	2.16

References

Alonso, Diego Hayashi, Garcia Rodriguez, Luis Fernando, and Silva, Emílio Carlos Nelli (2021). "Flexible framework for fluid topology optimization with OpenFOAM® and finite element-based high-level discrete adjoint method (FEniCS/dolfin-adjoint)", *Structural and Multidisciplinary Optimization*,

Alonso, Diego Hayashi *et al.*, (2022). "Topology optimization method based on the Wray-Agarwal turbulence model", *Structural and Multidisciplinary Optimization*, Vol. 65 No. 3, pp. 1–24.

Alonso, Diego Hayashi *et al.*, (2025). "Topology optimisation of transient compressible flow", *Engineering with Computers*,

Andreasen, Casper Schousboe, Gersborg, Allan Roulund, and Sigmund, Ole (2009). "Topology optimization of microfluidic mixers", *International Journal for Numerical Methods in Fluids*, Vol. 61, pp. 498–513.

Borrvall, Thomas and Petersson, Joakim (2003). "Topology optimization of fluids in Stokes flow", *International Journal for Numerical Methods in Fluids*, Vol. 41 No. 1, pp. 77–107. ISSN: 1097-0363.

CFD Online (2020). *Turbulence length scale*,

Chikh, Salah and Campo, Antonio (2005). "On the Maximization of Turbulent Free Convection along Heated Vertical Plates by Means of Preferable Gaseous Media", *Heat Transfer Research - HEAT TRANSF RES*, Vol. 36, pp. 247–265.

Cockburn, Bernardo and Shu, Chi-Wang (2001). "Runge–Kutta discontinuous Galerkin methods for convection-dominated problems", *Journal of scientific computing*, Vol. 16 No. 3, pp. 173–261.

COMSOL (2018). *CFD Module User's Guide, 5.4*, COMSOL.

Davis, Timothy A. (2004). "Algorithm 832: UMFPACK V4.3—an Unsymmetric-Pattern Multifrontal Method", *ACM Trans. Math. Softw.* Vol. 30 No. 2, pp. 196–199. ISSN: 0098-3500.

De Chant, Lawrence J. (2005). "The venerable 1/7th power law turbulent velocity profile: a classical nonlinear boundary value problem solution and its relationship to stochastic processes", *Journal of Applied Mathematics and Computational Mechanics*, Vol. 161, pp. 463–474.

Deng, Yongbo, Liu, Zhenyu, and Wu, Yihui (2013). "Topology Optimization of Steady and Unsteady Incompressible Navier—Stokes Flows Driven by Body Forces", *Struct. Multidiscip. Optim.* Vol. 47 No. 4, pp. 555–570. ISSN: 1615-147X.

Deng, Yongbo *et al.*, (2011). "Topology optimization of unsteady incompressible Navier–Stokes flows", *Journal of Computational Physics*, Vol. 230 No. 17, pp. 6688–6708.

Dilgen, Cetin B. *et al.*, (2018). "Topology optimization of turbulent flows", English. *Computer Methods in Applied Mechanics and Engineering*, Vol. 331, 363–393. ISSN: 0045-7825.

Farrell, Patrick E *et al.*, (2013). "Automated derivation of the adjoint of high-level transient finite element programs", *SIAM Journal on Scientific Computing*, Vol. 35 No. 4, pp. C369–C393.

Garcia Rodriguez, Luis Fernando, Alonso, Diego Hayashi, and Silva, Emílio Carlos Nelli (2025). "Turbulence effects in the topology optimization of compressible subsonic flow", *International Journal for Numerical Methods in Fluids*, Vol. 97 No. 1, pp. 44–68.

Gassner, Gregor J. and Winters, Andrew R. (2021). "A Novel Robust Strategy for Discontinuous Galerkin Methods in Computational Fluid Mechanics: Why? When? What? Where?", *Frontiers in Physics*, Vol. 8. ISSN: 2296-424X.

Gersborg-Hansen, Allan, Sigmund, Ole, and Haber, Robert B (2005). "Topology optimization of channel flow problems", *Structural and multidisciplinary optimization*, Vol. 30 No. 3, pp. 181–192.

Han, Xu, Rahman, Mizanur, and Agarwal, Ramesh K (2018). "Development and Application of Wall-Distance-Free Wray-Agarwal Turbulence Model (WA2018)", *2018 AIAA Aerospace Sciences Meeting*, p. 0593.

Han, Xu, Wray, Tim, and Agarwal, Ramesh K (2017). "Application of a new DES model based on wray-agarwal turbulence model for simulation of wall-bounded flows with separation", *47th AIAA Fluid Dynamics Conference*, p. 3966.

Hartmann, Ralf (2006). "Discontinuous Galerkin methods for compressible flows: higher order accuracy, error estimation and adaptivity", *VKI Lecture Series*, Vol. 0, pp. 1–50.

Hartmann, Ralf and Houston, Paul (2008). "An optimal order interior penalty discontinuous Galerkin discretization of the compressible Navier–Stokes equations", *Journal of Computational Physics*, Vol. 227 No. 22, pp. 9670–9685.

Hoellinger, Tristan, Chapelier, Jean-Baptiste, and Manueco, Lucas (2025). "A vorticity confinement correction for discontinuous Galerkin schemes applied to fluid flow problems", *International Journal of Numerical Methods for Heat & Fluid Flow*,

Houston, Paul and Sime, Nathan (2018). "Automatic symbolic computation for discontinuous Galerkin finite element methods", *SIAM Journal on Scientific Computing*, Vol. 40 No. 3, pp. C327–C357.

Jensen, Kristian Ejlebjerg, Szabo, Peter, and Okkels, Fridolin (2012). "Topology optimization of viscoelastic rectifiers", *Applied Physics Letters*, Vol. 100 No. 23, p. 234102.

Kreissl, Sebastian, Pingen, Georg, and Maute, Kurt (2011). "Topology optimization for unsteady flow", *International Journal for Numerical Methods in Engineering*, Vol. 87 No. 13, pp. 1229–1253.

Landet, Tormod, Mardal, Kent-Andre, and Mortensen, Mikael (2020). "Slope limiting the velocity field in a discontinuous Galerkin divergence-free two-phase flow solver", *Computers & Fluids*, Vol. 196, p. 104322. ISSN: 0045-7930.

Lazarov, Boyan Stefanov and Sigmund, Ole (2010). "Filters in topology optimization based on Helmholtz-type differential equations", *International Journal for Numerical Methods in Engineering*, Vol. 86 No. 6, pp. 765–781.

Lin, Sen *et al.*, (2015). "Topology optimization of fixed-geometry fluid diodes", *Journal of Mechanical Design*, Vol. 137 No. 8, 081402:1–081402:8.

Logg, Anders, Mardal, Kent-Andre, and Wells, Garth (2012). *Automated solution of differential equations by the finite element method: The FEniCS book*, Vol. 84. Springer Science & Business Media.

Maffei, Felipe Silva *et al.*, (2023). "Integer programming topology optimization for subsonic compressible flows with geometry trimming", *International Journal of Heat and Mass Transfer*, Vol. 201, p. 123614. ISSN: 0017-9310.

Makhija, David and Beran, Philip S (2019). "Time scale effects in topology optimization of the interior material distribution of a body subject to transient conjugate heat transfer", *AIAA Scitech 2019 Forum*, p. 1468.

Mitusch, Sebastian, Funke, Simon, and Dokken, Jørgen (2019). "dolfin-adjoint 2018.1: automated adjoints for FEniCS and Firedrake", *Journal of Open Source Software*, Vol. 4 No. 38, p. 1292.

Munson, Bruce R, Young, Donald F, and Okiishi, Theodore H (2009). *Fundamentals of fluid mechanics*, 6th ed. John Wiley & Sons, Inc.

Okubo, Carlos *et al.*, (2022). "A discrete adjoint approach based on finite differences applied to topology optimization of flow problems", *Computer Methods in Applied Mechanics and Engineering*, Vol. 389, p. 114406.

Papoutsis-Kiachagias, EM *et al.*, (2011). "Constrained topology optimization for laminar and turbulent flows, including heat transfer", *CIRA, editor, EUROGEN, Evolutionary and Deterministic Methods for Design, Optimization and Control, Capua, Italy*,

Pingen, Georg and Maute, Kurt (2010). "Optimal design for non-Newtonian flows using a topology optimization approach", *Computers & Mathematics with Applications*, Vol. 59 No. 7, pp. 2340–2350.

Pope, S. B. (2000). *Turbulent Flows*, Cambridge University Press. ISBN: 978-0521598866.

Rohde, Axel (2001). "Eigenvalues and eigenvectors of the Euler equations in general geometries", *15th AIAA Computational Fluid Dynamics Conference*, p. 2609.

Romero, J.S. and Silva, E.C.N. (2014). "A topology optimization approach applied to laminar flow machine rotor design", *Computer Methods in Applied Mechanics and Engineering*, Vol. 279 No. Supplement C, pp. 268 –300. ISSN: 0045-7825.

Sá, Luís Fernando Nogueira, Okubo Jr, Carlos Massaiti, and Silva, Emílio Carlos Nelli (2021). "Topology Optimization of Subsonic Compressible Flows", *Structural and Multidisciplinary Optimization*,

Schwedes, Tobias *et al.*, (2017). *Mesh dependence in PDE-constrained optimisation – An Application in Tidal Turbine Array Layouts*, 1st ed. Springer.

Sivapuram, R. and Picelli, R. (2018). "Topology optimization of binary structures using Integer Linear Programming", *Finite Elements in Analysis and Design*, Vol. 139, pp. 49–61. ISSN: 0168-874X.

Souza, Bruno Caldas *et al.*, (2021). "Topology optimization of fluid flow by using Integer Linear Programming", *Structural and Multidisciplinary Optimization*,

Weller, Henry G *et al.*, (1998). "A tensorial approach to computational continuum mechanics using object-oriented techniques", *Computers in physics*, Vol. 12 No. 6, pp. 620–631.

Wilcox, David C. (2006). *Turbulence Modeling for CFD*, 3rd ed. DCW Industries, Inc.

Wray, Tim and Agarwal, Ramesh K (2016). "Application of the Wray-Agarwal Model to Compressible Flows", *46th AIAA Fluid Dynamics Conference*, p. 3641.

Wray, Timothy J and Agarwal, Ramesh K (2015). "Low-Reynolds-Number One-Equation Turbulence Model Based on k-ω Closure", *AIAA Journal*, Vol. 53 No. 8, pp. 2216–2227.

Yaji, Kentaro *et al.*, (2016). "Topology optimization in thermal-fluid flow using the lattice Boltzmann method", *Journal of Computational Physics*, Vol. 307, pp. 355–377. ISSN: 0021-9991.

Yoon, Gil Ho (2016). "Topology optimization for turbulent flow with Spalart–Allmaras model", *Computer Methods in Applied Mechanics and Engineering*, Vol. 303, pp. 288 –311. ISSN: 0045-7825.

— (2020). "Topology optimization method with finite elements based on the k-ε turbulence model", *Computer Methods in Applied Mechanics and Engineering*, Vol. 361, p. 112784. ISSN: 0045-7825.

Zhang, Bin and Liu, Xiaomin (2015). "Topology Optimization Study of Arterial Bypass Configurations Using the Level Set Method", *Struct. Multidiscip. Optim.* Vol. 51 No. 3, pp. 773–798. ISSN: 1615-147X.

A Convergence evaluation

A convergence evaluation is presented in this section, by considering the energy dissipation eq. (21) for the initial guess topology of the U-bend configuration. Fig. 18 shows the computation of this function for different mesh discretisations. Note that the largest error happens for 5,490 elements, and is smaller than 6% afterwards. The impact of the errors from the CFD simulation in the optimisation process lies in the computation of the sensitivities. The computed sensitivities are illustrated in Fig. 19 for different mesh discretisations. Note that overall, the distributions are largely similar, indicating that the direction of the optimisation should be similar in all cases.

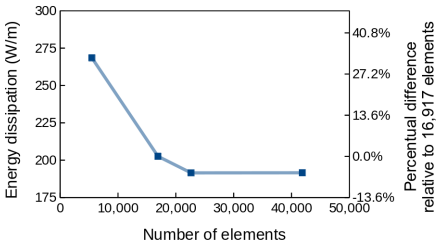

Figure 18: Energy dissipation values computed for different mesh discretisations (Source: Authors own work).

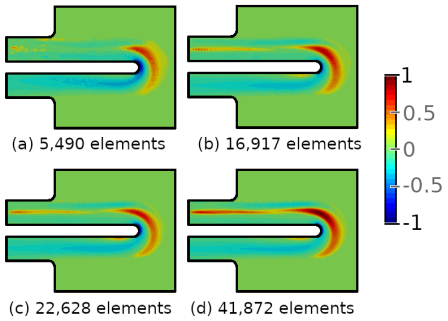

Figure 19: Sensitivities scaled by the cell sizes, and normalized between -1 and 1 (centered around the 0 value), for different mesh discretisations. Since the sensitivities naturally depend on the cell sizes, it is necessary to scale them when comparing different mesh discretisations, which is analogous to what is done when considering an L^2 Riesz map (Schwedes *et al.*, 2017) (Source: Authors own work).